

## SEARCHES FOR HIGH-FREQUENCY VARIATIONS IN THE $^8\text{B}$ SOLAR NEUTRINO FLUX AT THE SUDBURY NEUTRINO OBSERVATORY

B. AHARMIM<sup>1</sup>, S. N. AHMED<sup>2</sup>, A. E. ANTHONY<sup>3,20</sup>, N. BARROS<sup>4</sup>, E. W. BEIER<sup>5</sup>, A. BELLERIVE<sup>6</sup>, B. BELTRAN<sup>7</sup>, M. BERGEVIN<sup>8,9</sup>, S. D. BILLER<sup>10</sup>, K. BOUDJEMLINE<sup>6</sup>, M. G. BOULAY<sup>2</sup>, T. H. BURRITT<sup>11</sup>, B. CAI<sup>2</sup>, Y. D. CHAN<sup>8</sup>, D. CHAUHAN<sup>1</sup>, M. CHEN<sup>2</sup>, B. T. CLEVELAND<sup>10</sup>, G. A. COX<sup>11</sup>, X. DAI<sup>2,6,10</sup>, H. DENG<sup>5</sup>, J. DETWILER<sup>8</sup>, M. DIMARCO<sup>2</sup>, P. J. DOE<sup>11</sup>, G. DOUCAS<sup>10</sup>, P.-L. DROUIN<sup>6</sup>, C. A. DUBA<sup>11</sup>, F. A. DUNCAN<sup>2,12</sup>, M. DUNFORD<sup>5,21</sup>, E. D. EARLE<sup>2</sup>, S. R. ELLIOTT<sup>11,13</sup>, H. C. EVANS<sup>2</sup>, G. T. EWAN<sup>2</sup>, J. FARINE<sup>1,6</sup>, H. FERGANI<sup>10</sup>, F. FLEUROT<sup>1</sup>, R. J. FORD<sup>2,12</sup>, J. A. FORMAGGIO<sup>11,14</sup>, N. GAGNON<sup>8,10,11,13</sup>, J. TM. GOON<sup>15</sup>, K. GRAHAM<sup>2,6</sup>, E. GUILLIAN<sup>2</sup>, S. HABIB<sup>7</sup>, R. L. HAHN<sup>16</sup>, A. L. HALLIN<sup>7</sup>, E. D. HALLMAN<sup>1</sup>, P. J. HARVEY<sup>2</sup>, R. HAZAMA<sup>11,22</sup>, W. J. HEINTZELMAN<sup>5</sup>, J. HEISE<sup>2,13,17,23</sup>, R. L. HELMER<sup>18</sup>, A. HIME<sup>13</sup>, C. HOWARD<sup>7</sup>, M. A. HOWE<sup>11</sup>, M. HUANG<sup>1,3</sup>, B. JAMIESON<sup>17</sup>, N. A. JELLEY<sup>10</sup>, K. J. KEETER<sup>12</sup>, J. R. KLEIN<sup>3,5</sup>, L. L. KORMOS<sup>2</sup>, M. KOS<sup>2</sup>, C. KRAUS<sup>2</sup>, C. B. KRAUSS<sup>7</sup>, T. KUTTER<sup>15</sup>, C. C. M. KYBA<sup>5</sup>, J. LAW<sup>9</sup>, I. T. LAWSON<sup>9,12</sup>, K. T. LESKO<sup>8</sup>, J. R. LESLIE<sup>2</sup>, I. LEVINE<sup>6,24</sup>, J. C. LOACH<sup>8,10</sup>, R. MACLELLAN<sup>2</sup>, S. MAJERUS<sup>10</sup>, H. B. MAK<sup>2</sup>, J. MANEIRA<sup>4</sup>, R. MARTIN<sup>2,8</sup>, N. MCCAULEY<sup>5,10,25</sup>, A. B. McDONALD<sup>2</sup>, S. MCGEE<sup>11</sup>, M. L. MILLER<sup>14,26</sup>, B. MONREAL<sup>14,27</sup>, J. MONROE<sup>14</sup>, B. MORISSETTE<sup>12</sup>, B. G. NICKEL<sup>9</sup>, A. J. NOBLE<sup>2,6</sup>, H. M. O'KEEFFE<sup>10,28</sup>, N. S. OBLATH<sup>11</sup>, G. D. OREBI GANN<sup>5,10</sup>, S. M. OSER<sup>17</sup>, R. A. OTT<sup>14</sup>, S. J. M. PEETERS<sup>10,29</sup>, A. W. P. POON<sup>8</sup>, G. PRIOR<sup>8,30</sup>, S. D. REITZNER<sup>9</sup>, K. RIELAGE<sup>11,13</sup>, B. C. ROBERTSON<sup>2</sup>, R. G. H. ROBERTSON<sup>11</sup>, M. H. SCHWENDENER<sup>1</sup>, J. A. SECREST<sup>5,31</sup>, S. R. SEIBERT<sup>3,13</sup>, O. SIMARD<sup>6</sup>, D. SINCLAIR<sup>6,18</sup>, P. SKENSVED<sup>2</sup>, T. J. SONLEY<sup>14,32</sup>, L. C. STONEHILL<sup>11,13</sup>, G. TEŠIĆ<sup>6</sup>, N. TOLICH<sup>11</sup>, T. TSUI<sup>17</sup>, C. D. TUNNELL<sup>3</sup>, R. VAN BERG<sup>5</sup>, B. A. VANDEVENDER<sup>11</sup>, C. J. VIRTUE<sup>1</sup>, B. L. WALL<sup>11</sup>, D. WALLER<sup>6</sup>, H. WAN CHAN TSEUNG<sup>10,11</sup>, D. L. WARK<sup>19,33</sup>, P. J. S. WATSON<sup>6</sup>, N. WEST<sup>10</sup>, J. F. WILKERSON<sup>11,34</sup>, J. R. WILSON<sup>10,35</sup>, J. M. WOUTERS<sup>13</sup>, A. WRIGHT<sup>2</sup>, M. YEH<sup>16</sup>, F. ZHANG<sup>6</sup>, AND K. ZUBER<sup>10,36</sup>

<sup>1</sup> Department of Physics and Astronomy, Laurentian University, Sudbury, ON P3E 2C6, Canada

<sup>2</sup> Department of Physics, Queen's University, Kingston, ON K7L 3N6, Canada

<sup>3</sup> Department of Physics, University of Texas at Austin, Austin, TX 78712-0264, USA

<sup>4</sup> Laboratório de Instrumentação e Física Experimental de Partículas, Av. Elias Garcia 14, 1º, 1000-149 Lisboa, Portugal

<sup>5</sup> Department of Physics and Astronomy, University of Pennsylvania, Philadelphia, PA 19104-6396, USA

<sup>6</sup> Ottawa-Carleton Institute for Physics, Department of Physics, Carleton University, Ottawa, ON K1S 5B6, Canada

<sup>7</sup> Department of Physics, University of Alberta, Edmonton, Alberta, T6G 2R3, Canada

<sup>8</sup> Institute for Nuclear and Particle Astrophysics and Nuclear Science Division, Lawrence Berkeley National Laboratory, Berkeley, CA 94720, USA

<sup>9</sup> Physics Department, University of Guelph, Guelph, ON N1G 2W1, Canada

<sup>10</sup> Department of Physics, University of Oxford, Denys Wilkinson Building, Keble Road, Oxford OX1 3RH, UK

<sup>11</sup> Center for Experimental Nuclear Physics and Astrophysics, and Department of Physics, University of Washington, Seattle, WA 98195, USA

<sup>12</sup> SNOLAB, Sudbury, ON P3Y 1M3, Canada

<sup>13</sup> Los Alamos National Laboratory, Los Alamos, NM 87545, USA

<sup>14</sup> Laboratory for Nuclear Science, Massachusetts Institute of Technology, Cambridge, MA 02139, USA

<sup>15</sup> Department of Physics and Astronomy, Louisiana State University, Baton Rouge, LA 70803, USA

<sup>16</sup> Chemistry Department, Brookhaven National Laboratory, Upton, NY 11973-5000, USA

<sup>17</sup> Department of Physics and Astronomy, University of British Columbia, Vancouver, BC V6T 1Z1, Canada

<sup>18</sup> TRIUMF, 4004 Wesbrook Mall, Vancouver, BC V6T 2A3, Canada

<sup>19</sup> Rutherford Appleton Laboratory, Chilton, Didcot OX11 0QX, UK

Received 2009 October 13; accepted 2009 November 23; published 2010 January 20

### ABSTRACT

We have performed three searches for high-frequency signals in the solar neutrino flux measured by the Sudbury Neutrino Observatory, motivated by the possibility that solar  $g$ -mode oscillations could affect the production or propagation of solar  $^8\text{B}$  neutrinos. The first search looked for any significant peak in the frequency range  $1\text{--}144\text{ day}^{-1}$ , with a sensitivity to sinusoidal signals with amplitudes of 12% or greater. The second search focused on regions in which  $g$ -mode signals have been claimed by experiments aboard the *Solar and Heliospheric Observatory* satellite, and was sensitive to signals with amplitudes of 10% or greater. The third search looked for extra power across the entire frequency band. No statistically significant signal was detected in any of the three searches.

**Key words:** neutrinos – methods: data analysis – Sun: helioseismology

**Online-only material:** color figures

<sup>20</sup> Current address: Center for Astrophysics and Space Astronomy, University of Colorado, Boulder, CO, USA.

<sup>21</sup> Current address: Department of Physics, University of Chicago, Chicago, IL, USA.

<sup>22</sup> Current address: Department of Physics, Hiroshima University, Hiroshima, Japan.

<sup>23</sup> Current address: Sanford Laboratory at Homestake, Lead, SD, USA.

<sup>24</sup> Current address: Department of Physics and Astronomy, Indiana University, South Bend, IN, USA.

<sup>25</sup> Current address: Department of Physics, University of Liverpool, Liverpool, UK.

<sup>26</sup> Current address: Center for Experimental Nuclear Physics and Astrophysics, and Department of Physics, University of Washington, Seattle, WA, USA.

<sup>27</sup> Current address: Department of Physics, University of California, Santa Barbara, CA, USA.

<sup>28</sup> Current address: Department of Physics, Queen's University, Kingston, Ontario, Canada.

<sup>29</sup> Current address: Department of Physics and Astronomy, University of Sussex, Brighton, UK.

<sup>30</sup> Current address: CERN, Geneva, Switzerland.

## 1. INTRODUCTION

Neutrinos are the only way known to directly probe the dynamics of the solar core (Bahcall & Ulrich 1988), and, through the Mikheev–Smirnov–Wolfenstein (MSW) effect (Mikheev & Smirnov 1986; Wolfenstein 1977), they can even carry information about the rest of the solar envelope. To date, however, converting measurements of solar neutrino fluxes into constraints on solar models has proven to be difficult (Bandyopadhyay et al. 2007) because of the large number of co-varying parameters upon which such models are built.

A relatively simple signal that could tell us something new about the Sun would be a time variation in the neutrino fluxes. Over the past 40 years, measurements made by solar neutrino experiments have therefore been the focus of many studies, ranging from attempted correlations with the solar sunspot cycle to open searches for signals with periods of weeks or months (Sturrock 2003, 2004; Sturrock et al. 2005; Yoo et al. 2003; Aharmim et al. 2005a). The shortest period examined to date is roughly one day, where the MSW effect predicts that neutrinos propagating through the Earth’s core during the night will undergo flavor transformation in much the same way they do in the Sun, resulting in a net gain in the flux of electron neutrinos ( $\nu_e$ s). Although there have been occasional claims of signals on timescales similar to known variations in the solar magnetic field, in all cases there have been conflicting measurements that show the signals to be spurious or absent entirely.

We present in this paper the results of a search in a new frequency regime for solar time variations. Our focus has been on signals whose periods range from 24 hr down to 10 minutes. The motivation for such a high-frequency search is in part the expectation for solar helioseismological variations on scales of order an hour or less, in particular solar “gravity modes” ( $g$ -modes; Christensen-Dalsgaard 2003). These  $g$ -modes are non-radial oscillations that are predicted to be confined to the solar core, and thus could in principle affect either neutrino production or neutrino propagation. The neutrinos that Sudbury Neutrino Observatory (SNO) detects, those from  $^8\text{B}$  decay within the Sun, are particularly well suited for our search because they are created very deep within the solar core and because their propagation is known to be sensitive to variations in the solar density profile through the MSW effect.

The effects of  $g$ -modes on solar neutrino fluxes have been examined by Bahcall & Kumar (1993), who sought to determine whether  $g$ -mode effects could explain the apparent solar neutrino deficit, finding that any effect was far too small to account for the roughly 60% discrepancy. More recently, Burgess et al. (2003) looked at ways in which a broad spectrum of  $g$ -modes could alter the expectation for a solar neutrino spectral distortion caused by the MSW effect. Nevertheless, there are at this time no explicit predictions as to whether  $g$ -modes or any

other short-timescale variations could lead to measurable solar neutrino flux variations.

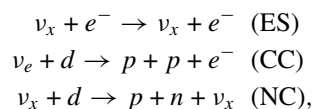
## 2. SUDBURY NEUTRINO OBSERVATORY

SNO was an imaging Cherenkov detector using heavy water ( $\text{D}_2\text{O}$ ) as both the interaction and detection medium (Boger et al. 2000). The SNO cavern is located in Vale Inco’s Creighton Mine, at  $46^\circ 28' 30''$  N latitude,  $81^\circ 12' 04''$  W longitude. The detector resided 1783 m below sea level with an overburden of  $5890 \pm 94$  m water equivalent, deep enough that the rate of cosmic-ray muons passing through the entire active volume was just three per hour.

One thousand metric tons of heavy water were contained in a 12 m diameter transparent acrylic vessel (AV). Cherenkov light produced by neutrino interactions and radioactive backgrounds was detected by an array of 9456 Hamamatsu model R1408 20 cm photomultiplier tubes (PMTs), supported by a stainless steel geodesic sphere (the PMT support structure or PSUP). Each PMT was surrounded by a light concentrator (a “reflector”), which increased the light collection to nearly 55%. Over 7 kilotonnes (7000 kg) of light water shielded the heavy water from external radioactive backgrounds: 1.7 kilotonnes between the acrylic vessel and the PMT support sphere, and 5.7 kilotonnes between the PMT support sphere and the surrounding rock. The 5.7 kilotonnes of light water outside the PMT support sphere were viewed by 91 outward-facing 20 cm PMTs that were used for identification of cosmic-ray muons.

The detector was equipped with a versatile calibration deployment system which could place radioactive and optical sources over a large range of the  $x$ - $z$  and  $y$ - $z$  planes in the AV. In addition, periodic “spikes” of short-lived radioactivity (such as  $^{222}\text{Rn}$ ) were added to both the light water and heavy water and distributed throughout their volumes to act as distributed calibration sources.

SNO detected neutrinos through three different processes as follows:



where  $\nu_x$  represents  $\nu_e$ ,  $\nu_\mu$  or  $\nu_\tau$ . For both the elastic scattering (ES) and charged current (CC) reactions, the recoil electrons were observed directly by their production of Cherenkov light. For the neutral current (NC) reaction, the neutrons were not seen directly, but were detected when they captured on another nucleus. In SNO Phase I (the “ $\text{D}_2\text{O}$  phase”), the neutrons captured on the deuterons present within the SNO heavy water. The capture on deuterium releases a 6.25 MeV  $\gamma$  ray, and it is the Cherenkov light of the secondary Compton electrons or  $e^+e^-$  pairs which was detected. In Phase II (the “salt phase”), 2 tonnes of NaCl were added to the heavy water, and the neutrons captured predominantly on  $^{35}\text{Cl}$  nuclei. Chlorine has a much larger capture cross section (resulting in a higher detection efficiency) for the neutrons. The capture on chlorine also yields multiple  $\gamma$ ’s instead of the single  $\gamma$  from the pure  $\text{D}_2\text{O}$  phase, which aids in the identification of neutron events.

Figure 1 shows the incident  $^8\text{B}$  spectrum of neutrinos from the Sun (dotted line), along with those that are detected by the CC reaction (dashed) and those that are above the effective kinetic energy threshold for the resultant electrons in our detector for Phase II,  $T_{\text{eff}} > 5.5$  MeV.  $T_{\text{eff}}$  is the estimated energy assuming an event consisted of a single electron.

<sup>31</sup> Current address: Department of Chemistry and Physics, Armstrong Atlantic State University, Savannah, GA, USA.

<sup>32</sup> Current address: Department of Physics, University of Utah, Salt Lake City, UT, USA.

<sup>33</sup> Additional address: Imperial College, London, UK.

<sup>34</sup> Current address: Department of Physics, University of North Carolina, Chapel Hill, NC, USA.

<sup>35</sup> Current address: Department of Physics, Queen Mary University, London, UK.

<sup>36</sup> Current address: Institut für Kern- und Teilchenphysik, Technische Universität Dresden, Dresden, Germany.

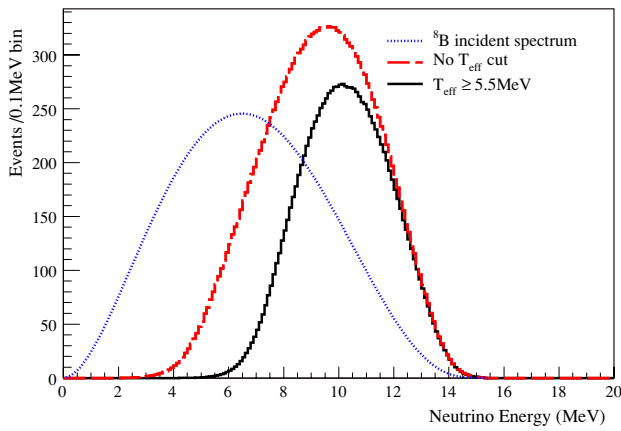


**Figure 1.** Monte Carlo simulation of the  $^8\text{B}$  solar neutrino energy spectrum. The dotted curve is the incident spectrum of neutrinos from the Sun with an arbitrary normalization, the dashed curve shows the spectrum of those detected by the CC reaction before any cut on the kinetic energy of the created electron, and the solid curve shows the spectrum of neutrinos seen after the application of the kinetic energy threshold for Phase II.

(A color version of this figure is available in the online journal.)

SNO's depth, very low radioactivity levels, and its ability to perform real-time detection made it a unique instrument for observing time variations in solar neutrino fluxes, even at the high frequencies we examine here. Above an energy threshold of 5 MeV, the rate of events from radioactivity, cosmic-ray muons, and atmospheric neutrinos, was negligible. The rate of solar neutrino events above this threshold was roughly  $10 \text{ day}^{-1}$ .

### 3. DATA SETS

The event selection for the data sets is similar to that used in our lower frequency periodicity analysis (Aharmim et al. 2005a). Events were selected inside a reconstructed fiducial volume of  $R < 550 \text{ cm}$  and above an effective kinetic energy of  $T_{\text{eff}} > 5 \text{ MeV}$  (Phase I) or  $T_{\text{eff}} > 5.5 \text{ MeV}$  (Phase II), and below  $T_{\text{eff}} > 20 \text{ MeV}$ . Additional analysis cuts such as fiducial volume and background rejection for these data sets have been described in detail elsewhere (Aharmim et al. 2007, 2005b). SNO Phase I ran between 1999 November 2 and 2001 May 31, and with detector dead times and periods of high radon removed, we recorded a total of 306.58 live days, with 2924 candidate neutrino events. SNO Phase II ran from 2001 July 26 to 2003 August 28 for a total of 391.71 live days and 4722 candidate neutrino events. Of the 2924 candidate events in the Phase I data, 67% are due to CC interactions, 20% due to NC interactions, and 9% due to ES interactions, with the remaining 4% due to backgrounds. Variations in the  $^8\text{B}$  neutrino production rate itself will affect all three neutrino interactions equally, while variations in the electron–neutrino survival probability dominantly affect only the CC rate. For the Phase II data, the 4722 events consist of 45% CC events, 42% NC events, 6% ES events, and 7% backgrounds.

The time for each event was measured with a global positioning system (GPS) clock to a resolution of  $\sim 100 \text{ ns}$ , but truncated to 10 ms accuracy for the analysis. The run boundary times were determined from the times of the first and last events in each run with a precision of  $\sim 50 \text{ ms}$ . The intervals between runs during which SNO was not recording solar neutrino events correspond to run transitions, detector maintenance, calibration activities, and any periods when the detector was off. It is also necessary to account for dead time incurred within a run; for example, dead

time due to spallation cuts that remove events occurring within 20 s after a muon. This is important for a high-frequency periodicity search, as the frequency of occurrence of these dead times can approach the scale of interest of our search. Therefore, both the run boundaries and the smaller, discrete breaks in time due to removal of short-lived backgrounds such as spallation products define the time exposure of the data set, which itself may induce frequency components that could affect a periodicity analysis.

### 4. RAYLEIGH POWER APPROACH

The low-frequency searches for periodicities that have been done by ourselves and others typically group the neutrino time series in bins of one to several days and then perform the analysis with methods such as the Lomb–Scargle technique (Yoo et al. 2003; Sturrock 2004). In our own low-frequency study (Aharmim et al. 2005a), we also used an unbinned maximum likelihood technique, fitting the time series with periodic functions of varying frequencies, phases, and amplitudes, allowing for the detector dead times that occurred during calibration runs, power outages, and detector maintenance.

For this high-frequency study, we chose to use an unbinned Rayleigh power approach. The Rayleigh power of a time series for a given frequency  $\nu$  is defined as

$$z(\nu) \equiv \frac{U(\nu)^2}{N} = \frac{1}{N} [(\sum_i \cos 2\pi \nu t_i)^2 + (\sum_i \sin 2\pi \nu t_i)^2], \quad (1)$$

where  $N$  is the total number of events in the time series.

The great advantage of the Rayleigh power approach is its speed, as it requires far fewer function evaluations than other unbinned methods like the maximum likelihood technique described above. For this analysis, speed is critical, because to ensure that we do not miss a signal we use 1.6 million equally spaced frequencies spanning a range from  $1\text{--}144 \text{ day}^{-1}$  (one cycle per 10 minutes). To avoid the possibility of a signal falling between our sampled frequencies, and thus being missed, the minimum gap between our sampled frequencies must correspond to two signals that just decorrelate over the course of SNO's running period. With this criterion, the minimum number of frequencies needed for our data set in our region of interest is 400,000, and our choice of 1.6 million frequencies was made to provide a small degree of oversampling.

For a time series in which the phase coverage is uniform, the distribution of Rayleigh powers for any given frequency follows  $e^{-z}$ , and thus confidence intervals can be easily calculated. For the SNO data set, there are significant dead-time intervals, whose durations range from months to milliseconds. The sources of these dead-time intervals include the period between the Phase I and Phase II data sets (several months), detector calibration runs (typically hours to days), power outages (of order one day), maintenance periods (hours), and offline veto periods (15 ms to 20 s) imposed to remove events associated with the passage of cosmic-ray muons through the detector, interactions of atmospheric neutrinos, or bursts of instrumental activity.

The dead-time structure of the SNO time series means that not all phases of the Rayleigh power are equally likely, and thus leads to additional Rayleigh power that is not associated with any neutrino signal. Quasi-periodic dead times (like those associated with calibration and maintenance) can also lead to peaks in the Rayleigh power spectrum. To calculate confidence intervals in order to determine the significance of any peaks observed in the Rayleigh power spectrum, we must account for these known regions of non-uniform phase coverage.

We have developed an analytic model for the Rayleigh power at a given frequency by treating the Rayleigh power series as a two-dimensional random walk. Each detected event is treated as a step in the random walk, with components  $X = \cos 2\pi \nu t$  and  $Y = \sin 2\pi \nu t$ . For the case of uniform phase coverage, the central limit theorem implies that for a large number of steps ( $N$ ) the distribution of final positions will be given by a two-dimensional Gaussian, whose means, variances, and covariance are

$$\mu_x = \frac{1}{2\pi} \int_0^{2\pi} d\phi \cos \phi = 0 \quad (2)$$

and

$$\sigma_x^2 = \frac{1}{2\pi} \int_0^{2\pi} d\phi \cos^2 \phi = \frac{1}{2} \quad (3)$$

$$\text{cov}(x, y) = \frac{1}{2\pi} \int_0^{2\pi} d\phi \cos \phi \sin \phi = 0 \quad (4)$$

leading to a simple distribution of final positions given by

$$\begin{aligned} f(X, Y) &= \frac{1}{2\pi N \sigma_x \sigma_y} \exp(-X^2/2N\sigma_x^2) \exp(-Y^2/2N\sigma_y^2) \\ &= \frac{1}{N\pi} e^{-(X^2+Y^2)/N} \\ &= \frac{1}{N\pi} e^{-U^2/N}. \end{aligned}$$

The distribution of  $z = U^2/N$  can then be obtained by integrating over all values of  $X$  and  $Y$  which satisfy  $z < U^2/N < z + dz$  by changing variables from  $X$  and  $Y$  to  $\psi$  and  $U$ :

$$f(X, Y) dX dY \rightarrow f(U, \psi) dU d\psi = \frac{1}{N\pi} e^{-U^2/N} U dU d\psi. \quad (5)$$

Integrating this expression over  $d\psi$  from 0 to  $2\pi$  and changing variables from  $U$  to  $z = U^2/N$  gives  $f(z) dz = e^{-z} dz$ , which is the simple exponential distribution expected for the Rayleigh power distribution.

For the case of non-uniform coverage, the means and covariance of the distribution are no longer simple. If we call the normalized phase-weighting function  $g(\phi)$ , where  $g(\phi) = 1$  for uniform phase coverage, then we have

$$\mu_x = \frac{1}{2\pi} \int_0^{2\pi} d\phi g(\phi) \cos \phi \quad (6)$$

$$\mu_y = \frac{1}{2\pi} \int_0^{2\pi} d\phi g(\phi) \sin \phi \quad (7)$$

$$\sigma_x^2 = \frac{1}{2\pi} \int_0^{2\pi} d\phi g(\phi) (\cos \phi - \mu_x)^2 \quad (8)$$

$$\sigma_y^2 = \frac{1}{2\pi} \int_0^{2\pi} d\phi g(\phi) (\sin \phi - \mu_y)^2 \quad (9)$$

$$\text{cov}(x, y) = \frac{1}{2\pi} \int_0^{2\pi} d\phi g(\phi) (\cos \phi - \mu_x)(\sin \phi - \mu_y). \quad (10)$$

The function  $g(\phi)$  is determined by the detector's dead-time window, with  $\phi = \omega t$ . The mean for  $X$ , for example, is given by

$$\mu_x = \frac{1}{T} \sum_{j=1}^{\text{runs}} \int_{t_{\text{start},j}}^{t_{\text{stop},j}} dt \cos \omega t, \quad (11)$$

where  $T$  is the total live time, and the sum is over all data taking runs in the data set, integrating from the start to the stop time of each run.

The Rayleigh power distribution for the non-uniform phase coverage case is proportional to  $e^{-\chi^2/2}$ , and  $\chi^2$  for the Rayleigh power distribution can be written as

$$\chi^2(X, Y) = (X - N\mu_x, Y - N\mu_y) V_{xy}^{-1} \begin{pmatrix} X - N\mu_x \\ Y - N\mu_y \end{pmatrix}. \quad (12)$$

The inverse of the covariance matrix is given by  $V_{xy}^{-1} = \begin{pmatrix} N\sigma_x^2 & N\text{cov}(x, y) \\ N\text{cov}(x, y) & N\sigma_y^2 \end{pmatrix}^{-1}$  making our  $\chi^2$ ,

$$\chi^2 = \frac{(X - N\mu_x)^2 \sigma_y^2 + (Y - N\mu_y)^2 \sigma_x^2 - 2(X - N\mu_x)(Y - N\mu_y) \text{cov}(x, y)}{N\sigma_x^2 \sigma_y^2 - N\text{cov}^2(x, y)}. \quad (13)$$

Transforming into our integration variables  $z = U^2/N$ , and  $\psi$  gives the rather unwieldy probability density function for the Rayleigh power at a given frequency:

$$f(z) dz = \frac{1}{C} dz \int_0^{2\pi} e^{-(\alpha_1(\psi)/2)Nz - (\alpha_2(\psi)/2)N\sqrt{Nz} - (\alpha_3(\psi)/2)N^2} d\psi, \quad (14)$$

where

$$\begin{aligned} \alpha_1(\psi) &= \sigma_y^2 \cos^2 \psi + \sigma_x^2 \sin^2 \psi - 2 \cos \psi \sin \psi \text{cov}(x, y) \\ \alpha_2(\psi) &= -2(\sigma_y^2 \mu_x \cos \psi + \sigma_x^2 \mu_y \sin \psi \\ &\quad + (\mu_x \sin \psi + \mu_y \cos \psi) \text{cov}(x, y)) \\ \alpha_3(\psi) &= \sigma_y^2 \mu_x^2 + \sigma_x^2 \mu_y^2 + \mu_x \mu_y \text{cov}(x, y) \end{aligned}$$

and  $C$  is a normalization constant. In this formalism, the effects of detector dead time are entirely accounted for through the means and covariance matrix for the variables  $X$  and  $Y$ . In the analysis of data from the two combined SNO data-taking phases, the difference in event rates between Phase I and Phase II is accounted for by separating the terms of the analytic form according to phase, or

$$N\mu_{x,y} \rightarrow N_{D_2} \mu_{x,y} + N_{\text{Salt}} \mu_{x,y}$$

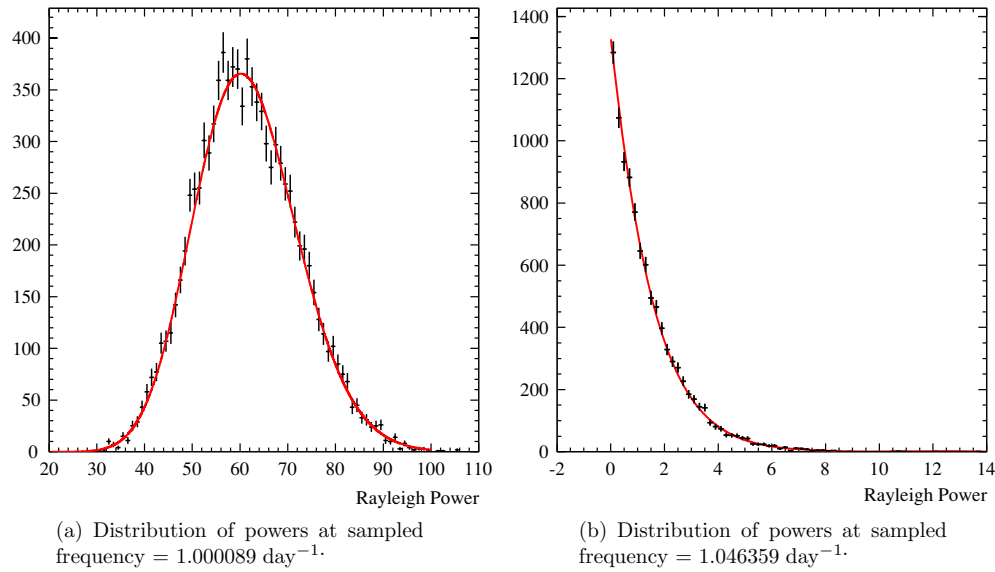
(and similarly for all variance and covariance terms). Here, both  $g(\phi)$  and  $N$  have been separated according to phase, effectively introducing a rate-dependent weighting factor. For further details on this method, see Anthony (2008).

Figure 2 shows the function  $f(z)$  describing the Rayleigh power distributions for two different frequencies. The distributions were generated with a Monte Carlo simulation including the SNO detector's full dead-time window. For the plot on the left, the dead time contributes a significant amount of power due to the periodicity in SNO's operations schedule, while for the high-frequency bin on the right the dead time does not change the function much from its simple  $e^{-z}$  distribution.

To determine a specific confidence level, CL, for a given observed Rayleigh power,  $z_0$ , we solve the equation

$$\text{CL} = \int_0^{z_0} f(z) dz. \quad (15)$$





**Figure 2.** Distribution of specific frequencies’ Rayleigh powers in SNO Monte Carlo data sets (black) vs. the predictive analytic form (red line). (a) Distribution of powers at sampled frequency = 1.000089 day<sup>-1</sup>. (b) Distribution of powers at sampled frequency = 1.046359 day<sup>-1</sup>.

(A color version of this figure is available in the online journal.)

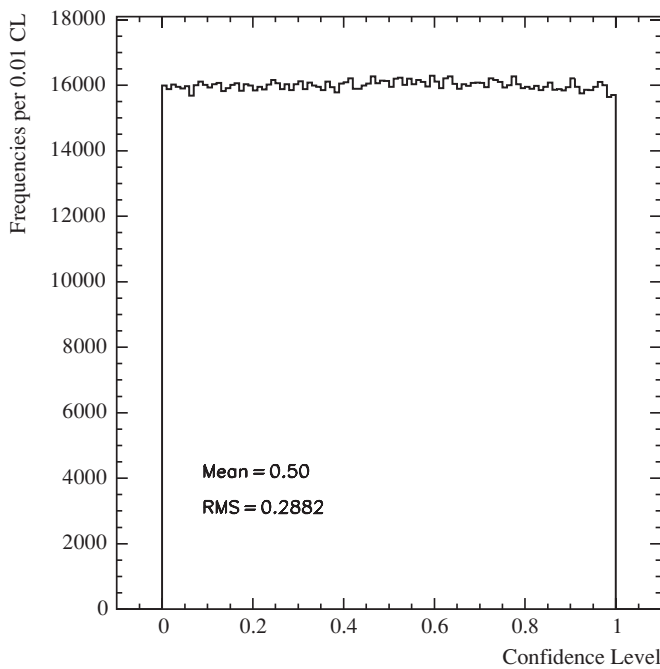


**Figure 3.** Distribution of Rayleigh power confidence levels for all frequencies of a Monte Carlo simulation of the SNO data set.

As a test of our analytic model, we have calculated the confidence levels for all 1.6 million frequencies of a Monte Carlo simulation that includes the full SNO dead-time window. Figure 3 shows the distribution of these confidence levels, which is gratifyingly flat with a mean that is 0.50, thus showing that the analytic random walk model correctly distributes the confidence levels across the whole Rayleigh power spectrum.

### 5. OPEN SINGLE PEAK SEARCH

Our first search looked for a significant peak at any frequency in our Rayleigh power spectrum. While Equation (15) gives the confidence level at any specific frequency, when testing our

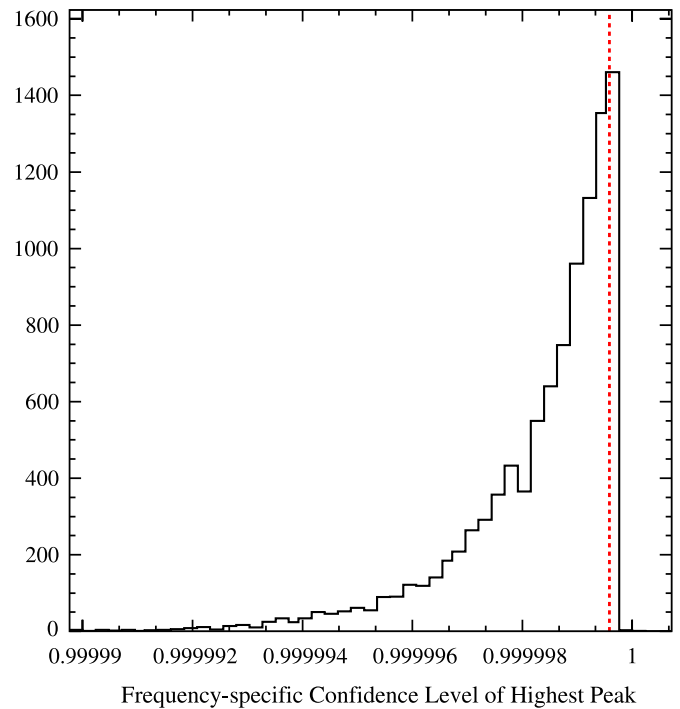


**Figure 4.** Distribution of maximum confidence levels from Rayleigh analysis of 10,000 signal-free Monte Carlo data sets. By building this distribution of maximum confidence levels, we can determine a “confidence level of confidence levels” and account for the trials penalty in our generation of the data-wide confidence level. The frequency-specific confidence level corresponding to the data-wide confidence level of 90% is shown with the dashed red line.

(A color version of this figure is available in the online journal.)

1.6 million sampled frequencies there is a substantial trials penalty, making it exceedingly likely that at least one of the frequencies will by chance have an apparently large power. To determine this penalty exactly, we would need to know how many of our 1.6 million sampled frequencies are independent, which is a complex task.

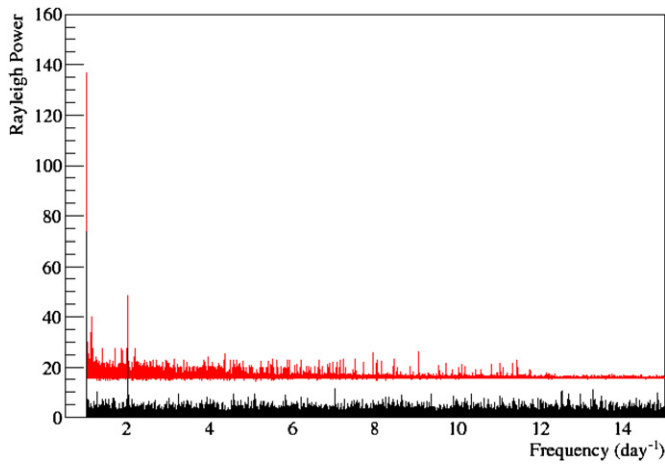


**Figure 5.** Rayleigh power spectra for first subsection (frequencies between 1 and 15  $\text{day}^{-1}$ ) of the entire range of frequencies sampled (from 1 to 144  $\text{day}^{-1}$ ) for combined SNO Phase I and Phase II data sets. The entire range has been broken down into six individual frames for easier inspection, with the first frame slightly more zoomed-in due to the presence of more underlying activity in this region of lower frequencies. The black line indicates data, and the upper red line designates the level at which a detection would have a confidence level of 90%. The peaks at low frequencies, specifically those at 1  $\text{day}^{-1}$  and 2  $\text{day}^{-1}$ , represent SNO-specific periodicities due to daily run-taking schedules. (This is clearly not evidence of a signal, as the red CL = 90% line, generated from null-hypothesis Monte Carlo, also follows these peaks.)

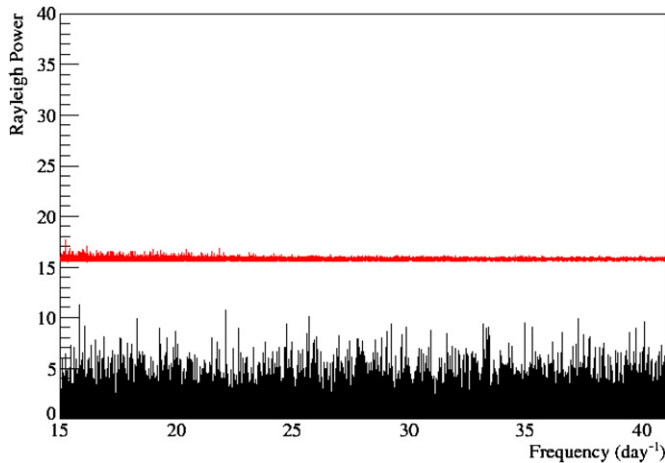


**Figure 6.** Rayleigh power spectra for second subsection (frequencies between 15 and 41  $\text{day}^{-1}$ ) of the entire range of frequencies sampled (from 1 to 144  $\text{day}^{-1}$ ) for combined SNO Phase I and Phase II data sets. The black line indicates data, and the upper red line designates the level at which a detection would have a confidence level of 90%.

Instead, to address this trials penalty we use 10,000 null-hypothesis Monte Carlo simulations to determine the probability of observing a statistically significant peak at any of the 1.6 million sampled frequency in the absence of a true signal. For a given null-hypothesis Monte Carlo simulation, we assign a frequency-specific confidence level to each sampled frequency according to the prescription given in Section 4 (see Equation (15)). Then for each null-hypothesis Monte Carlo simulation, we record the peak that has the highest confidence level, and then plot the resultant distribution of these highest peak confidence levels for all 10,000 null-hypothesis Monte Carlo simulations. The resultant distribution of confidence levels is shown in Figure 4. As seen from this figure, virtually every simulation yields at least one peak with an apparent significance of at least 99.999%, just by chance. To determine the true data-wide confidence level, taking into account our entire

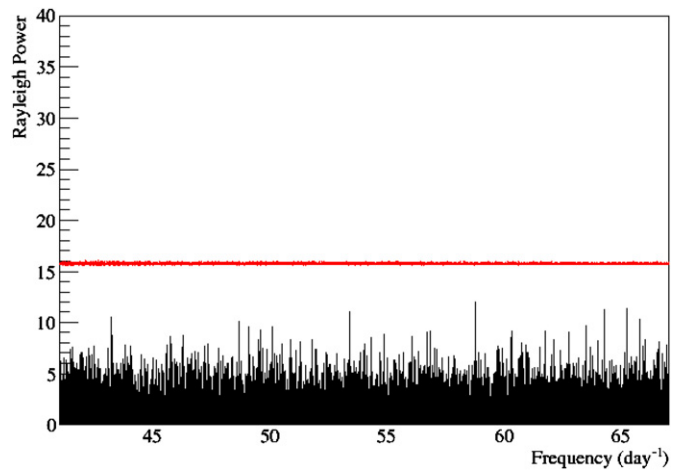


**Figure 7.** Rayleigh power spectra for third subsection (frequencies between 41 and 67  $\text{day}^{-1}$ ) of the entire range of frequencies sampled (from 1 to 144  $\text{day}^{-1}$ ) for combined SNO Phase I and Phase II data sets. The black line indicates data, and the upper red line designates the level at which a detection would have a confidence level of 90%.

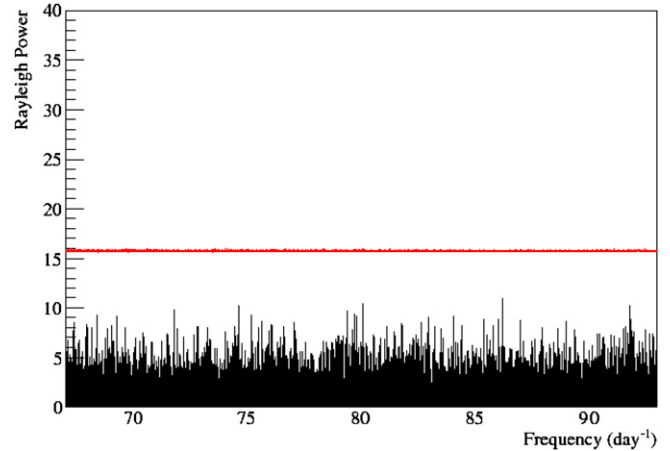


**Figure 8.** Rayleigh power spectra for fourth subsection (frequencies between 67 and 93  $\text{day}^{-1}$ ) of the entire range of frequencies sampled (from 1 to 144  $\text{day}^{-1}$ ) for combined SNO Phase I and Phase II data sets. The black line indicates data, and the upper red line designates the level at which a detection would have a confidence level of 90%.

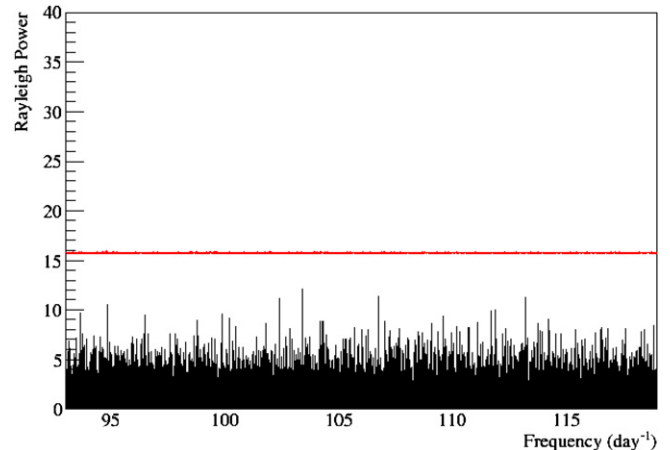


**Figure 9.** Rayleigh power spectra for fifth subsection (frequencies between 93 and 119  $\text{day}^{-1}$ ) of the entire range of frequencies sampled (from 1 to 144  $\text{day}^{-1}$ ) for combined SNO Phase I and Phase II data sets. The black line indicates data, and the upper red line designates the level at which a detection would have a confidence level of 90%.

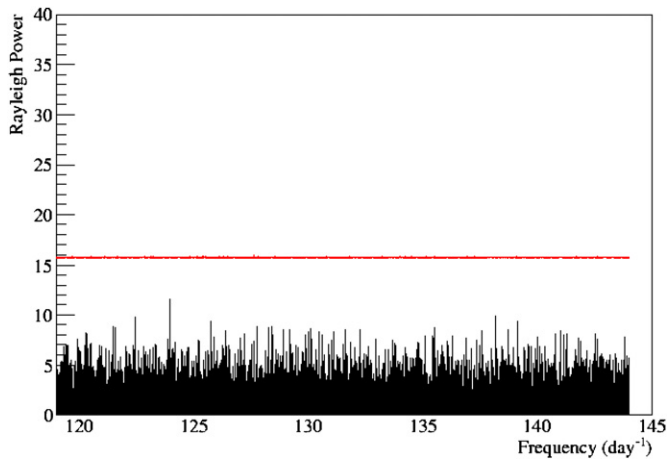


**Figure 10.** Rayleigh power spectra for sixth subsection (frequencies between 119 and 144  $\text{day}^{-1}$  of the entire range of frequencies sampled (from 1 to 144  $\text{day}^{-1}$ , for combined SNO Phase I and Phase II data sets). The black line indicates data, and the upper red line designates the level at which a detection would have a confidence level of 90%.

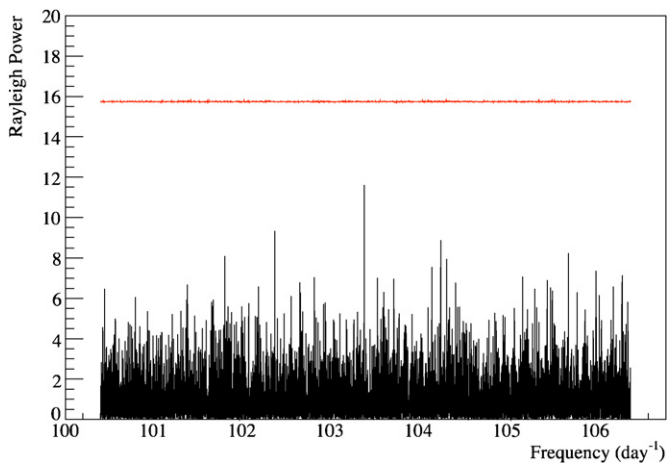


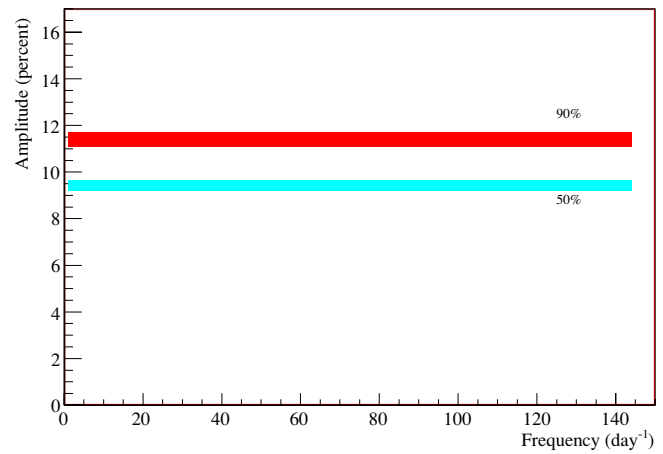
**Figure 11.** Zoomed-in region of the Rayleigh power spectrum for the highest significance peak in the SNO data set, which was detected at frequency= $103.384 \text{ day}^{-1}$ , with a confidence level of 2%. The horizontal red line indicates the frequency-specific powers needed for a peak to be above the data-wide 90% CL.

sample of 1.6 million frequencies, we place a cut on the distribution of Figure 4 that corresponds to our desired trials-weighted (data-wide, rather than frequency-specific) confidence level for a significant signal. In Figure 4, the cut shown corresponds to the frequency-specific confidence level needed by the maximum peak in a power spectrum in order for it to be above the 90% CL detection threshold. In other words, for a data set that contains no periodicity at any frequency, there is a less than 10% probability that the most significant individual peak will have a frequency-specific confidence level in excess of this cut value.

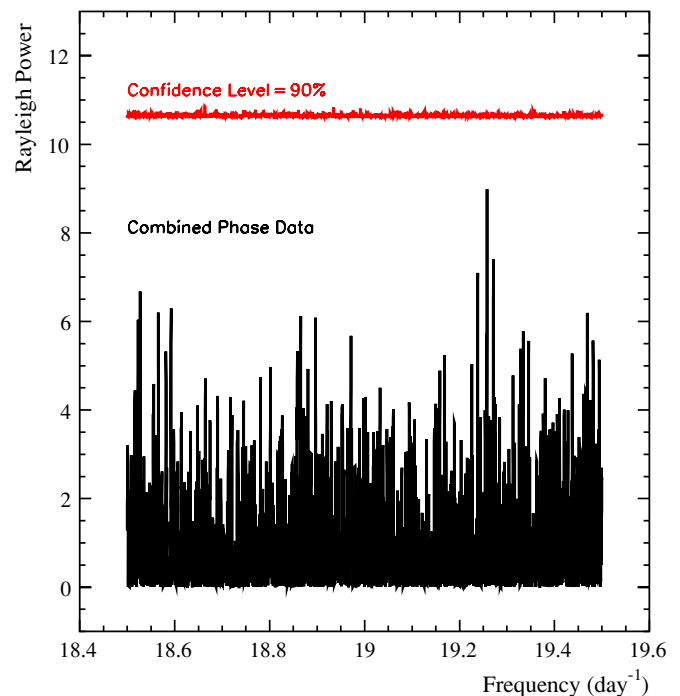
Figures 5 through 10 show the Rayleigh power spectrum for the combined SNO Phase I and Phase II data sets, broken up into six segments each corresponding to roughly 267,000 sampled frequencies.

Figure 11 shows the peak with the highest confidence level, and the corresponding threshold for that peak to be above the data-wide 90% CL to be considered significant. The data-wide CL of this peak is only 2%; thus, we see no evidence of a significant peak in our data set.

To determine our sensitivity to a signal, we ran Monte Carlo simulations with fake sinusoidal signals of form  $1 + A \sin \omega t$ , of



**Figure 12.** SNO's sensitivities to a high-frequency periodic signal in the combined data sets (Phase I, or  $\text{D}_2\text{O}$ , and Phase II, or salt) for the entire frequency search region. The lower (cyan) band shows the calculated sensitivity at which we detect a signal 50% of the time, with 99% CL, and the upper (red) band shows the calculated sensitivity at which we detect a signal 90% of the time, with 99% CL. The width of the bands represents the range of variation of the sensitivity, which varies rapidly with frequency, across the frequency regime.



**Figure 13.** Rayleigh power spectrum for “directed” high-frequency search, in black. The line corresponding to detection with 90% CL is shown in red. The highest peak in the power spectrum is found at a frequency of  $19.2579 \text{ day}^{-1}$  with a CL of 58%.

increasing amplitude, looking for the point at which our method would claim a discovery. In Figure 12, we show our sensitivity for two criteria: the amplitude required to make a 99% CL discovery 90% of the time, and the amplitude for a 99% CL discovery 50% of the time. We are substantially limited in this open search by the trials penalty; we need a signal of 12% amplitude to make a 99% CL detection 90% of the time. The bands shown in Figure 12 indicate the degree of variation among frequencies of the sensitivity, which is affected by the underlying power spectrum in each bin as discussed above in Section 4.

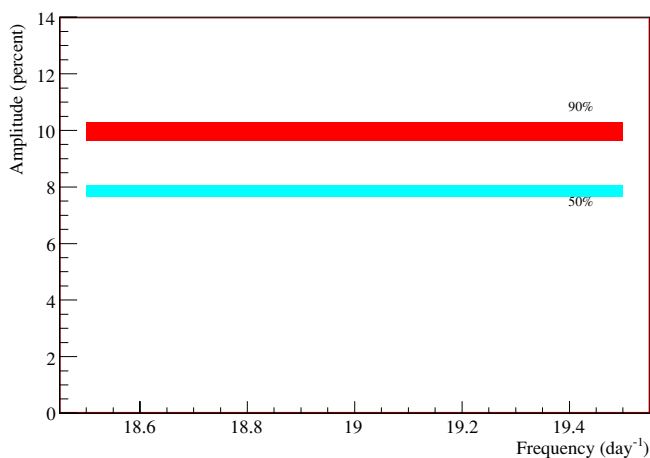


**Figure 14.** SNO’s sensitivities to a high-frequency periodic signal in the combined data sets (Phase I, or  $\text{D}_2\text{O}$ , and Phase II, or salt) for the directed high-frequency search region. The lower (cyan) band shows the calculated sensitivity at which we detect a signal 50% of the time, with 99% CL, and the upper (red) band shows the calculated sensitivity at which we detect a signal 90% of the time, with 99% CL. The width of the bands represents the range of variation of the sensitivity, which varies rapidly with frequency, across the frequency regime.

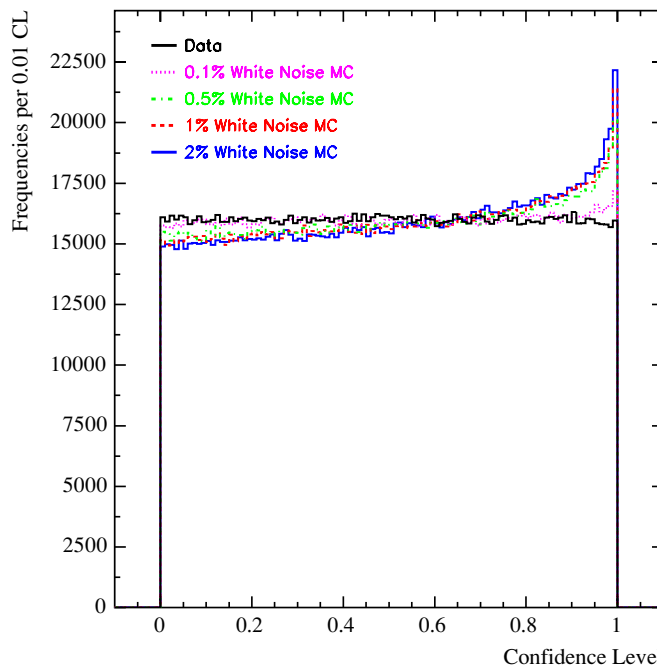


**Figure 16.** Distribution of confidence levels for all 1.6 million frequencies in a SNO white-noise Monte Carlo, with several signal amplitudes. The SNO combined-phase ( $\text{D}_2\text{O}$  and salt) data confidence level distribution is shown in black for comparison.

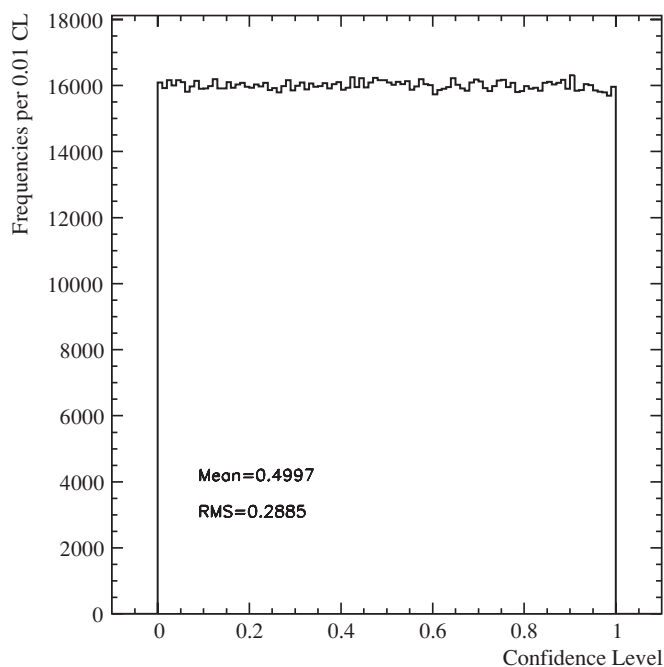


**Figure 15.** Distribution of confidence levels for all 1.6 million frequencies, for the SNO combined-phase ( $\text{D}_2\text{O}$  and salt) data set.

## 6. DIRECTED PEAK SEARCH

There have been recent claims by the  $\text{GOLF}^{37}/\text{SOHO}$  collaboration of possible signatures of  $g$ -mode oscillations based on analyses of long-term helioseismological data sets (García et al. 2001; Gabriel et al. 2002; Turck-Chièze et al. 2004; Mathur et al. 2007) as well as supporting claims by the  $\text{VIRGO}^{38}/\text{SOHO}$  collaboration (García et al. 2008). Looking for such specific signals in our data set using our Rayleigh power approach has an advantage in that we no longer need the 1.6 million frequencies used above, but rather can look in a narrow window that has a

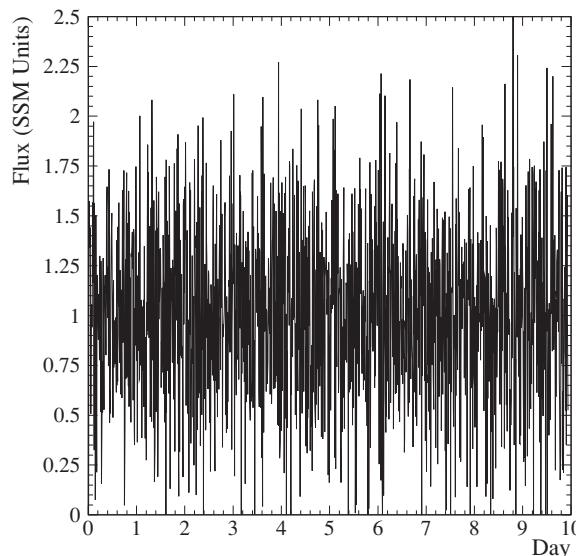


**Figure 17.** Time domain plot of our Gaussian white-noise model, with amplitude of 0.1%, distributed over 400,000 frequencies. Only 10 days are shown here. The rms noise power for the model shown here is 0.45 in units of SNO’s measured total  $^8\text{B}$  neutrino flux.

smaller trials penalty. We have thus taken a narrow band around the reported persistent  $\text{GOLF}$  signals (Jiménez & García 2009), from 18.5 to 19.5  $\text{day}^{-1}$  (roughly 214 to 225  $\mu\text{Hz}$ ), and have repeated our analysis. We again find no significant signal, with the highest peak having a trials-weighted CL of just 58%. The Rayleigh power spectrum around this peak, as well as its superimposed 90% CL are shown in Figure 13. Figure 14 shows our sensitivity plots for this directed search, which are slightly better than in Section 5 because of the reduced trials penalty. We conclude that if the detection claimed by  $\text{SOHO}$  is in fact evidence of a  $g$ -mode, the effect of this particular mode of oscil-

<sup>37</sup> Global Oscillations at Low Frequency.

<sup>38</sup> Variability of solar IRradiance and Gravity Oscillations.



lation on the neutrino flux is less than 10% amplitude variation, at 99% CL.

## 7. BROADBAND SEARCH

The two searches described above require that the signal be predominantly sinusoidal and monotonic. It is possible that high-frequency behavior in the Sun spans a large band of frequencies, and in fact may be “noisy.” Burgess et al. (2003) have investigated how such noise might affect the neutrino survival probabilities within the Sun due to the matter or MSW effect. We have therefore looked at the distribution of confidence levels across our entire range of 1.6 million frequencies. Like Figure 3, we expect that in the case of no broadband signal the distribution of confidence levels will be flat, with a mean of 0.50. Figure 15 shows this distribution now for our combined SNO Phase I and Phase II data sets. As can be seen clearly in the figure, the distribution is flat, with a mean very close to the 0.5 expected. As a comparison case, we show in Figure 16 what the confidence level distribution of a “noisy” Sun would look like for several different amplitudes of Gaussian white noise. Our white-noise model is shown in Figure 17 for the lowest amplitude (0.1%) shown in Figure 16. We have spread the noise across 400,000 independent frequencies, roughly the number of independent frequencies we expect in the power spectrum. The rms noise power from our model is 0.45, in units of SNO’s measured total  $^8\text{B}$  neutrino flux ( $\sim 5 \times 10^6 \nu \text{ cm}^{-2} \text{ s}^{-1}$ ). In terms of power per unit bandwidth, this corresponds to  $\sim 6 \times 10^7 \nu \text{ cm}^{-2} \text{ s}^{-1} \text{ Hz}^{-1/2}$ . As is evident in Figure 15, the distribution of confidence levels in the data is consistent with no distortion of signal due to noise.

## 8. CONCLUSIONS

We have performed three searches for high-frequency signals in the  $^8\text{B}$  solar neutrino flux, applying a Rayleigh power technique to data from the first two phases of SNO. Our first search looked for any significant peak in a Rayleigh power spectrum from frequencies ranging from 1 to 144  $\text{day}^{-1}$ . To account for SNO’s dead-time window, we calculated the expected distribution of power in each bin of the Rayleigh power spectrum using a random walk model, thus allowing us to assign confidence levels to the observed powers. We found no significant peaks in the data set. For this “open” peak search, we had a 90% probability of making a 99% CL detection of a signal with an amplitude of 12% or greater, relative to SNO’s time-averaged neutrino flux.

In a second search, we narrowed our frequency band to focus on a region in which  $g$ -mode signals have been claimed by experiments aboard the *SOHO* satellite. The examined frequency range extended from 18.5 to 19.5  $\text{day}^{-1}$ . Again, no

significant peaks in the Rayleigh power spectrum were found, and our sensitivity for this “directed” search gave us a 90% probability of making a 99% CL detection for signals whose amplitudes were 10% or larger, relative to SNO’s time-averaged neutrino flux.

Our third search examined the entire range of frequencies from 1 to 144  $\text{day}^{-1}$ , looking for any evidence that additional power was present across the entire high-frequency band. To do this, we used the distribution of frequency-specific confidence levels, determined using our random walk model. We found that, as expected for no high-frequency variations, this distribution was flat. We showed that for a simple Gaussian white-noise model, the confidence level distribution would be notably distorted even when the amplitudes of the contributing frequencies have an rms as small as 0.1%.

This research was supported by Canada: Natural Sciences and Engineering Research Council, Industry Canada, National Research Council, Northern Ontario Heritage Fund, Atomic Energy of Canada, Ltd., Ontario Power Generation, High Performance Computing Virtual Laboratory, Canada Foundation for Innovation; US: Dept. of Energy, National Energy Research Scientific Computing Center; UK: Science and Technologies Facilities Council. We thank the SNO technical staff for their strong contributions. We thank Vale Inco, Ltd. for hosting this project.

## REFERENCES

- Aharmim, B., et al. SNO Collaboration 2005a, *Phys. Rev. D*, **72**, 052010  
 Aharmim, B., et al. SNO Collaboration 2005b, *Phys. Rev. C*, **72**, 055502  
 Aharmim, B., et al. SNO Collaboration 2007, *Phys. Rev. C*, **75**, 045502  
 Anthony, A. E. 2008, PhD thesis, Univ. of Texas  
 Bahcall, J., & Kumar, P. 1993, *ApJ*, **409**, L73  
 Bahcall, J., & Ulrich, R. 1988, *Rev. Mod. Phys.*, **60**, 297  
 Bandyopadhyay, A., Choubey, S., Goswami, S., & Petcov, S. T. 2007, *Phys. Rev. D*, **75**, 093007  
 Boger, J., et al. SNO Collaboration 2000, *Nucl. Instrum. Methods A*, **449**, 172  
 Burgess, C. P., et al. 2003, *ApJ*, **588**, L65  
 Christensen-Dalsgaard, J. 2003, Lecture Notes on Stellar Oscillations (Århus: Inst. for Fysik og Astron.), <http://www.phys.au.dk/~jcd/oscilnotes/>  
 Gabriel, A. H., et al. 2002, *A&A*, **390**, 1119  
 García, R. A., et al. 2001, *Solar Phys.*, **200**, 361  
 García, R. A., et al. 2008, *Astron. Nachr.*, **329**, 476  
 Jiménez, A., & García, R. A. 2009, *ApJS*, **184**, 288  
 Mathur, S., Turck-Chièze, S., Couvidat, S., & García, R. A. 2007, *ApJ*, **668**, 594  
 Mikheev, S. P., & Smirnov, A. Y. 1986, *Nuovo Cimento C*, **9**, 17  
 Sturrock, P. 2003, *ApJ*, **594**, 1102  
 Sturrock, P. 2004, *ApJ*, **605**, 568  
 Sturrock, P. A., Caldwell, D. O., Scargle, J. D., & Wheatland, M. S. 2005, *Phys. Rev. D*, **72**, 113004  
 Turck-Chièze, S., et al. 2004, *ApJ*, **604**, 455  
 Wolfenstein, L. 1977, *Phys. Rev. D*, **17**, 2369  
 Yoo, J., et al. (Super-Kamiokande Collaboration) 2003, *Phys. Rev. D*, **68**, 092002